A&A 405, 833–849 (2003)
DOI: 10.1051/0004-6361:20030661

Astronomy & Astrophysics

A deep 6.7 μm survey in the SSA13 field with ISO⋆

Y. Sato[1,2], K. Kawara[2], L. L. Cowie[3], Y. Taniguchi[4], D. B. Sanders[3,7], H. Matsuhara[1], H. Okuda[5], K. Wakamatsu[6], Y. Sofue[2], R. D. Joseph[3], and T. Matsumoto[1]

[1] Institute of Space and Astronautical Science (ISAS), 3-1-1 Yoshinodai, Sagamihara, Kanagawa 229-8510, Japan
[2] Institute of Astronomy, University of Tokyo, 2-21-1 Osawa, Mitaka, Tokyo 181-0015, Japan
[3] Institute for Astronomy, University of Hawaii, 2680 Woodlawn Drive, Honolulu, HI 96822, USA
[4] Astronomical Institute, Graduate School of Science, Tohoku University, Aramaki, Aoba, Sendai 980-8578, Japan
[5] Gunma Astronomical Observatory, 6860-86 Nakayama, Takayama, Agatsuma, Gunma 377-0702, Japan
[6] Faculty of Engineering, Gifu University, 1-1 Yanagido, Gifu 501-1193, Japan
[7] Max-Planck Institut fur Extraterrestrische Physik, 85740 Garching, Germany

Received 29 August 2001 / Accepted 18 April 2003

Abstract. We present results of a deep mid-infrared survey in the SSA13 field with the Infrared Space Observatory (ISO). In order to probe the near-infrared light at high redshifts, we surveyed the field with the broad band *LW*2 (5–8.5 μm) filter of the mid-infrared camera ISOCAM. Adopting a highly redundant imaging strategy for the 23 h observation and carefully treating gradual changes in the detector responsivity caused by a very high rate of cosmic ray impacts, we succeeded in reaching an 80% completeness limit of 16 μJy in the central 7 arcmin^2 region. Utilizing the signal-to-noise ratio map, we detected 65 sources down to 6 μJy in the 16 arcmin^2 field. Integral galaxy number counts at 6.7 μm are then derived, reaching 1.3×10^4 deg^{-2} at the faint limit with a slope of -1.6 between 13 μJy and 130 μJy. Integrating individual sources in this flux range, the resolved fraction of the extragalactic background light at 6.7 μm is estimated to be 0.56 nW m^{-2} sr^{-1}. These results, which reach a flux limit three times fainter than those in the Hubble Deep Fields, are in fairly good agreement with a model prediction by Franceschini et al. (1997). Finally, we discuss the relation of distant massive E/S0 galaxies to the faint 6.7 μm galaxy population.

Key words. Galaxy: evolution – infrared: galaxies – cosmology: observations – surveys – galaxies: photometry – methods: data analysis

1. Introduction

Explorations of the evolution of galaxies require representative galaxy samples at high redshifts. Intrinsically sensitive optical observations succeeded in picking up $z \sim 3$ sources utilizing characteristic breaks in galaxy spectra (Steidel et al. 1996). Another technique to search for high redshift galaxies is to observe at wavelengths long-ward of a global peak in spectral energy distributions (SEDs) of galaxies. A famous example is the recent discovery of distant dusty starbursting galaxies in the Submillimeter and millimeter with the Submillimeter Common-User Bolometer Array SCUBA (Smail et al. 1997; Barger et al. 1998; Hughes et al. 1998) and the Max-Planck Millimeter Bolometer array MAMBO (Bertoldi et al. 2000). At submillimeter and millimeter wavelengths, contributions from foreground objects are small, since their dust emission has a peak around 100 μm and decreases toward longer wavelengths. On the other hand, contributions from higher redshift objects become greater because of the K-correction brightening; the rest-frame 100 μm dust peak shifts into the submillimeter or millimeter observing band with increasing redshift. As a result, the fraction of high redshift objects in the submillimeter or millimeter is greater than that at, say, 200 μm.

The same technique can be applied to another striking peak around 1 μm originating from stellar photospheres. The observing wavelength should be much longer than 1 μm to get the K-correction brightening. However, emission from PAH molecules and very hot dust should also be considered. Their contributions begin to increase at wavelengths long-ward of 6 μm for local objects. We selected the broad band *LW*2 filter at 6.7 μm in the mid-infrared camera ISOCAM (Cesarsky et al. 1996) as a good window between local stellar and dust emission. The fraction of high redshift objects would be larger at 6.7 μm than at 2.2 μm.

Previous field galaxy surveys at 6.7 μm were carried out in the Hubble Deep Field (HDF) and the Lockman Hole (Serjeant et al. 1997; Taniguchi et al. 1997). These found a few tens of 6.7 μm sources down to 30 μJy (Goldschmidt et al. 1997),

Send offprint requests to: Y. Sato,
e-mail: ysato@ioa.s.u-tokyo.ac.jp

⋆ Based on observations with ISO, an ESA project with instruments funded by ESA Member States (especially the PI countries: France, Germany, The Netherlands and the UK) and with the participation of ISAS and NASA.

Table 1. Properties of the ISOCAM observations in the individual revolutions. Column 1 is the revolution number counted since ISO's launch. Column 2 is the total target-dedicated-time (TDT) in a single revolution. Column 3 is the roll angle of the satellite, counted counterclockwise from north to the raster *N*-direction. Column 4 is the solar aspect angle between the target and the Sun. Column 5 is the measured sky brightness derived with the sensitivity parameter of 2.32 ± 0.08 ADU/G/s/mJy for the *LW*2 band (Blommaert 1998). ISOCAM signals in units of ADU/G/s (Analog-to-Digital Unit/Gain/second) can be converted to flux densities with the sensitivity parameter of the filter used. Column 6 is the lens position following the definition by Aussel et al. (1999). Columns 7 and 8 are the measured offsets between the ISOCAM detector and the nominal center of the ISOCAM field-of-view determined by the telescope. They are shown in the raster *M*- and *N*-directions in units of pixels. These shifts were caused by the jitter in the lens wheel repositioning (Sect. 2.2).

Revolution	Observing time (s)	Roll angle (deg)	Solar aspect angle (deg)	Sky (MJy sr^{-1})	Lens position	Offset in *M* (pix)	Offset in *N* (pix)
560	11 214	315.2	102.0	2.90	left	0.95	−0.24
561	11 214	314.4	101.4	2.94	right	−1.10	−0.10
610	15 315	279.9	69.2	4.11	left	1.21	0.16
612	15 315	278.4	68.1	4.21	left	0.90	−0.12
613	15 315	277.6	67.4	4.28	right	−0.97	0.19
614	15 315	276.7	66.8	4.19	right	−0.80	0.14

some of which were confirmed by re-calibration of the HDF data (Désert et al. 1999; Aussel et al. 1999). A more shallow (>100 μJy) survey was conducted in the CFRS field (Flores et al. 1999). An attempt to detect a field population lensed by a massive cluster lens was also performed at 6.7 μm (Altieri et al. 1999), reaching a faint detection limit comparable to those of the HDF and the Lockman Hole. Most recently, a survey of the HDF-South (HDF-S; Oliver et al. 2002) has been reported with the same depth as that of the HDF.

Here we present a very deep ISOCAM *LW*2 galaxy survey in the SSA13 field. We first describe the observing strategy (Sect. 2) and the data processing (Sect. 3). After evaluating the detection procedure by simulations (Sect. 4), we present the catalog of detected sources (Sect. 5). Finally we discuss the galaxy number counts and extragalactic background light (Sect. 6). Other properties of the individual sources will be described elsewhere (Sato et al. 2003).

2. Observation

2.1. Field selection

Small Selected Area 13 (SSA13), one of the Hawaii Deep Fields, was chosen as our deep 6.7 μm survey target. It is located at high galactic and ecliptic latitudes ($b \sim 74°$ and $\beta \sim 46°$) and has a very low atomic hydrogen column density of $N(\mathrm{H\,I}) = 1.5 \times 10^{20}$ cm^{-2} (Cowie et al. 1994). Owing to these attractive properties for extragalactic studies, SSA13 has become one of the most-studied regions of the sky, comparably with the HDFs. It has photometric data obtained not only in the optical and near-infrared, but also at submillimeter and X-ray wavelengths (Cowie et al. 1996; Barger et al. 1998, 1999; Mushotzky et al. 2000). A number of spectra were taken with the Low Resolution Imaging Spectrometer (LRIS) of the Keck telescope in a certain portion of the SSA13 field (Cowie et al. 1996). Because of the presence of a bright star ($R = 10.4$), the survey area was chosen to be the largest square region which is most distant from the star but inside the rectangular LRIS strip. The center of the region is (RA, Dec) = ($13^{\mathrm{h}}12^{\mathrm{m}}26\overset{\mathrm{s}}{.}0$, $42°44'24\overset{''}{.}8$) in J2000.

2.2. Observing strategy

The survey observations were conducted with the mid-infrared camera ISOCAM (Cesarsky et al. 1996) on board the Infrared Space Observatory ISO (Kessler et al. 1996). The sensitive broad band *LW*2 (5–8.5 μm) filter with a reference wavelength 6.7 μm (Moneti et al. 1997) was selected to detect radiation from stellar photospheres at high redshift. All the images were taken in the microscanning mode, CAM01, to minimize the flatfielding error (Siebenmorgen et al. 1996). Total target-dedicated-time (TDT) for the observations was 23 h.

Because of the visibility constraints for the SSA13 field, our observations were divided over six revolutions between revolution 560 and 614, 29 May 1997 and 22 Jul. 1997 in UT (Table 1). The observing time in each revolution was divided into two or three raster observations (Table 2). The observations were executed essentially in two runs separated by a 1.5 month interval, during which time the image plane of the spacecraft rotated about 45 degrees (cf. roll angles in Table 1). The main aim was to achieve better sampling of source profiles and also to maximize the overlapped area coverage.

The surface density of bright sources suitable for image registration was expected to be low at 6.7 μm. Thus, it was almost mandatory to fully utilize the unvignetted field-of-view for ISOCAM, 3 arcmin in diameter. We then selected the lens providing a 6 arcsec pixel field-of-view on the 32×32 pixel *LW* detector array. However, the use of 6 arcsec lens could introduce errors in the registration and hence degrade the depth of the map, because 6 arcsec pixels undersample the instrumental beam. At 6.7 μm, the diffraction limited beam size is 2.3 arcsec *FWHM* (Full Width at Half Maximum) for the 60 cm ISO mirror. In order to suppress this undersampling effect, we applied several raster step sizes corresponding to non-integer multiples of the detector pixel size (Table 2).

Table 2. Raster parameters used for the individual ISOCAM observations. Column 1 is the TDT number, the unique identification number for ISO observations. Columns 2 and 3 are the numbers of raster points in the raster *M*- and *N*-directions. The raster directions were fixed in the spacecraft coordinate system. Columns 4 and 5 are the raster step sizes. Note the pixel field-of-view was set to 6 arcsec.

TDTNR	*M*	*N*	ΔM (arcsec)	ΔN (arcsec)
560 001 01	6	6	7	7
560 001 02	3	2	9	9
561 003 03	6	6	7	7
561 003 04	3	2	9	9
610 005 05	6	6	7	7
610 005 06	4	4	8	8
610 005 07	3	2	9	9
612 001 08	6	6	7	7
612 001 09	4	4	8	8
612 001 10	3	2	9	9
613 002 11	6	6	7	7
613 002 12	4	4	8	8
613 002 13	3	2	9	9
614 003 14	6	6	7	7
614 003 15	4	4	8	8
614 003 16	3	2	9	9

Because of the likely faintness of sources that could be used as references for the image registration, all the raster observations in a single revolution were executed as a concatenated chain. If we had not adopted this concatenation setting, we could not align the CAM images and it would result in null results. In the concatenated chain, the nominal automatic transition to the standby mode between observations was suppressed. That transition, if permitted, would have introduced strong transients in the detector responsivity and random and systematic displacements of the image on the detector (Siebenmorgen et al. 1996). In fact, non-negligible displacements were actually identified among revolution maps taken with different lens positions (Table 1).

The integration time per exposure was set to $T_{\rm int} = 20$ s. With shorter integration time, data would have been dominated by the readout noise of the detector because of very low background emission at 6.7 μm. The number of exposures per raster position was chosen to be $N_{\rm exp} = 12$, following a caveat for robust cosmic ray rejection (Siebenmorgen et al. 1996). The number of stabilization exposures was set to $N_{\rm stab} = 21$ for the first raster in each revolution. The stabilization exposures were used as a buffer for the associated strong transients from the standby mode. Here the worst case was assumed, in which an observation would be preceded by a dark (zero flux) condition. For the subsequent rasters in any given revolution, the minimum stabilization value $N_{\rm stab} = 4$ was used, since no change in background illumination would occur in the concatenated chains. The analog-to-digital converter gain was set to the maximum ×4 to cope with the low contrast of faint sources on the background.

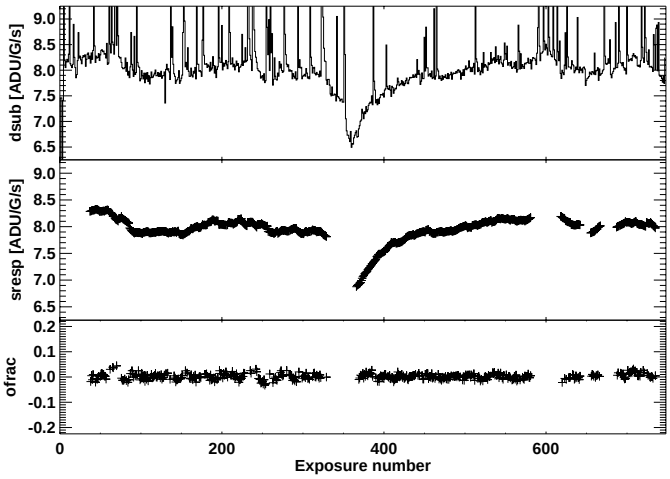

Fig. 1. An example of the responsivity correction to ISOCAM data taken with $T_{\rm int} = 20$ s. The top panel shows the dark-subtracted data $dsub = a\,(I_{\rm sky} + I_{\rm obj})$. The middle is $sresp = a\,I_{\rm sky}$, the response to the blank sky after cosmic ray and object masking. The bottom shows $ofrac = I_{\rm obj}/I_{\rm sky}$ after correcting the responsivity drifts. For the *sresp* and *ofrac* panels, bad portions are masked out. The bad portions are cosmic rays themselves and portions where good linear interpolations are impossible with cosmic rays-masked and object-masked *dsub* data (Appendices A.3.3, A.4).

3. Image processing

Mid-infrared data with ISOCAM suffer from cosmic rays (top panel of Fig. 1). There is a huge number of spikes in the pixel histories and the signals slowly change even when the background is constant. The latter is attributed to gradual changes or drifts in the detector responsivity due to the large number of cosmic ray impacts. Adopting the cosmic ray masking and the responsivity correction to deal with the above effects, we have done the data processing following the scheme outlined below. Details of these steps are described in Appendix A. They are coded as our own software.

For each detector pixel, its raw signal *raw* can be written as the linear equation

$$raw = a\,(I_{\rm sky} + I_{\rm obj}) + b, \quad (1)$$

where a is the responsivity, b is the dark signal, and $I_{\rm sky}$ and $I_{\rm obj}$ are fluxes from the sky and objects received by that pixel, respectively. The dark-subtracted signal *dsub* (top panel of Fig. 1) is then obtained as

$$dsub = raw - b \quad (2)$$

$$= a\,(I_{\rm sky} + I_{\rm obj}). \quad (3)$$

The sky signal $a\,I_{\rm sky}$ can be extracted by masking the object signal $a\,I_{\rm obj}$ and also cosmic rays (Appendices A.3.2, A.4). This manipulation $f(dsub)$ is essentially a linear interpolation of *dsub* signals applying the object and cosmic ray masks. The outcome reflects the detector response to the constant sky flux.

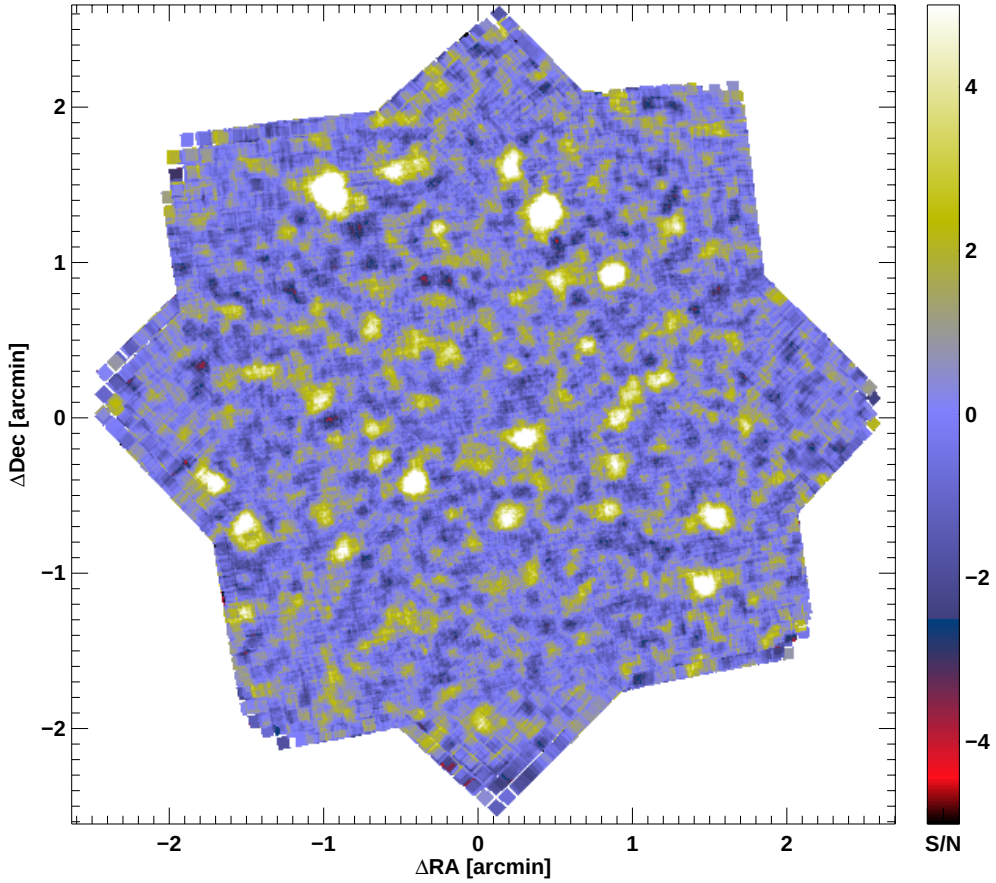

Fig. 2. The final map coadding all the data. North is top and east to the left in J2000. The center is (RA, Dec) = ($13^h12^m26\overset{s}{.}0, 42°44'24\overset{''}{.}8$). The map shows signal-to-noise ratio (*S/N*) per 0.6 arcsec sub-pixel. The signal is an average, weighted by the inverse of the assigned variance, and the noise is a normalized standard deviation (Sect. 3). (This figure is available in color in electronic form.)

We call it *sresp* (middle panel of Fig. 1),

$$sresp = f(dsub) \quad (4)$$
$$= a\, I_{\rm sky}, \quad (5)$$

and this will be used to correct the responsivity drifts. Then, the time-dependent responsivity a can be canceled out with the division of *dsub* by *sresp*,

$$dsub/sresp = 1 + I_{\rm obj}/I_{\rm sky}. \quad (6)$$

Thus, the fraction of the object flux *ofrac* can be given as

$$ofrac = I_{\rm obj}/I_{\rm sky} \quad (7)$$
$$= dsub/sresp - 1. \quad (8)$$

This technique for the responsivity correction works very well, resulting in a drastic reduction of noise (cf. bottom panel of Fig. 1).

Although $I_{\rm sky}$ is constant in time, each detector pixel has a different $I_{\rm sky}$ due to the optical distortion (Aussel 1998) and vignetting in the *LW* array. Let the pixel receive α times larger sky flux than the fiducial pixel. Then,

$$I_{\rm sky} = \alpha\, I^0_{\rm sky}, \quad (9)$$

where $I^0_{\rm sky}$ is the sky flux for the fiducial pixel. The fiducial sky flux $I^0_{\rm sky}$ is derived from the central part of the detector (Appendix A.5). Then the *ofrac* data are transferred to the object flux *obj* normalized to the fiducial pixel,

$$obj = ofrac \times I^0_{\rm sky} \quad (10)$$
$$= I_{\rm obj}/\alpha. \quad (11)$$

Deriving the conversion factor for the fiducial pixel, we can obtain real object fluxes from the *obj* data.

After calculating the *obj* data for all pixels, we made a map. To fully utilize the information of the raster positions and the optical distortion, we used sub-pixels of 0.6 arcsec to create a map from the *obj* data (Appendix A.6). After some iterations to refine the responsivity corrections with the cosmic ray and object masks and the offsets among revolutions, the final map was created. Figure 2 shows the final map in the form of signal-to-noise ratio (*S/N*). The *obj* signals were co-added with weights of their inverse variances which were calculated by tracing the error propagation from the *dsub* stage (Appendix A.2). Here we normalized standard deviations in sub-pixels in the coaddition so that the central part of the histogram of the *S/N*s in sub-pixels should resemble a Gaussian distribution with a sigma of one, because the noises in sub-pixels are correlated. There was no indication of a strong source confusion in the histogram, supporting the use of a Gaussian fit to the histogram (Appendix A.7).

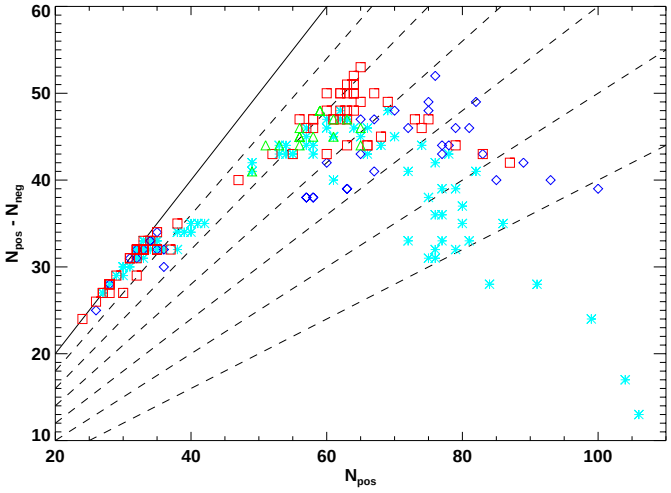

Fig. 3. A search for the detection parameters (Sect. 4.1). The parameters for source detections are: the surface brightness threshold, the number of 0.6 arcsec sub-pixels above the threshold, and the *FWHM* of the convolution Gaussian filter. Diamonds denote a Gaussian *FWHM* of 3 sub-pixels, asterisks 4 sub-pixels, squares 5 sub-pixels, and triangles 6 sub-pixels. A peak in $N_{\rm pos} - N_{\rm neg}$ moves toward lower $N_{\rm pos}$ with the larger *FWHM*, which corresponds to the suppression of noise detections. The lines indicate the detection reliability $(N_{\rm pos} - N_{\rm neg})/N_{\rm pos} = 100\%$ (solid line), 90, 80, 70, 60, 50, and 40% (dashed lines from the left to the right). (This figure is available in color in electronic form.)

4. Object extraction

4.1. Determination of the detection parameters

For extracting sources, the SExtractor program (Bertin & Arnouts 1996) was applied to Fig. 2, the final *S/N* map. The number of detected sources depends on three parameters: the surface brightness threshold, the number of 0.6 arcsec sub-pixels above the threshold, and the width of the Gaussian filter used to convolve the map.

The detection parameters were determined by comparing numbers of detected sources on the *S/N* map with those on the negative *S/N* map ($N_{\rm pos}$ and $N_{\rm neg}$, respectively). The negative *S/N* map was made by multiplying the *S/N* map by −1. Any detections made on the negative map are spurious, and no such sources should be detected (i.e. $N_{\rm neg} = 0$) where *S/N* is very high. The source extractions on the positive and negative maps were performed for more than 200 sets of the detection parameter values. The results are shown as a plot of $N_{\rm pos} - N_{\rm neg}$ against $N_{\rm pos}$ in Fig. 3.

For a perfect Gaussian noise field with positive source populations, $N_{\rm pos} - N_{\rm neg}$ should increase with $N_{\rm pos}$ up to a certain level and then flatten out at some $N_{\rm pos}$, where the noise begins to be detected. In fact, Fig. 3 shows a declining trend where the flattening is expected. This indicates that the number of noise sources are somewhat larger in the negative side. One explanation may be due to our technique for responsivity correction (Sect. 3). A failure in masking an object or a cosmic ray will result in two dips in the neighboring data. Such dips are actually identified around some bright sources in the final map (Fig. 2). We believe that at least three dips are related to sources #54, #57, and #22 (Table 3). Thus, their detection significance would be somewhat higher than the nominal values.

We chose the detection parameters which gave the maximum of $N_{\rm pos} - N_{\rm neg}$: 1.04 in the normalized *S/N* in sub-pixels for the surface brightness threshold, 119 sub-pixels above the threshold, and 5 sub-pixels for the width of the Gaussian. This parameter set resulted in $N_{\rm pos} = 65$ and $N_{\rm neg} = 12$. These values give a nominal detection reliability of 82% for the whole sample. However, the true detection reliability would be somewhat higher as indicated by the decreasing trend in Fig. 3.

4.2. Simulations of the detection procedure

4.2.1. Detection completeness

Monte Carlo simulations were performed to evaluate the completeness of the source detection. For each simulation, a single test source was added to the real data, the *S/N* map (Fig. 2). The profile of the test sources was fixed as a two dimensional Gaussian function. Its *FWHM* was determined by the real data; the intensity weighted average of the two smallest *FWHM*s among the ten most significant detections. It was 12 sub-pixels or 7.2 arcsec.

Since we used the *S/N* map in the detection, we assigned *S/N*s to the test sources with the random signal values. The noise was calculated for the 7.2 arcsec beam as a quadratic sum of the sub-pixel noises in that beam. This noise should be rescaled, because the sub-pixel noises are not independent. The scaling factor was determined so that the histogram of the *S/N*s in the 7.2 arcsec beam calculated over the entire map should be a Gaussian with a sigma of one. Thus, the noise includes all contributions from real sources (Barger et al. 1999). The *S/N*s were then determined with these signal and noise values.

The simulations were done with almost 50 000 sets of random *S/N*s and positions for test sources. As we used the real data, we set some conditions for detections; test sources should be detected within a distance of the *FWHM* and the excess of the measured fluxes over the assigned ones should be less than the assigned fluxes. In the case that a test source was added near a certain real source, some offset would be expected. However, if the offset becomes larger than the *FWHM*, this detection should be due to the pre-existing real source. Similarly, if the excess of the measured flux becomes larger than the assigned flux, such a detection should be related to pre-existing real source contributions. The result of the simulations is shown in Fig. 4. One sigma errors were estimated as Poissonian (Gehrels 1986). The completeness of the detection is about 50% and 80% at assigned *S/N*s of 2.5 and 4, respectively.

4.2.2. Positional errors

Figure 5 presents the simulation results for the offsets of the measured coordinates from the assigned ones. The offset is larger at lower *S/N*, and is larger than the expected values given by the formula $\sigma_{\rm pos} = FWHM/\sqrt{8\ln 2}/(S/N)$ (dashed line; Condon 1997). A similar formula was used for a submillimeter map with a high source density of 1/11 sources per beam

Table 3. The catalog of ISOCAM *LW*2 sources in the SSA13 field. Column 1 is the identification number. Columns 2 and 3 are the Right Ascension in hours, minutes, seconds and the declination in degrees, arcmins, arcsecs in the J2000 system. Column 4 is the total astrometric error (one sigma) in arcsec. It is a quadratic sum of the absolute astrometric error and the relative astrometric error calculated with 0.2 dex bins in Fig. 5. Column 5 is the normalized noise for the 7.2 arcsec diameter aperture at the source position. For its deviation, see Sect. 4.2.1. For the correction from instrumental values, a sensitivity parameter of 2.32 ADU/G/s/mJy is used (Blommaert 1998). Column 6 is the *LW*2 band (5–8.5 μm) flux in μJy. This is the total flux with all the flux corrections applied: the flux bias (Sect. 4.2.3), aperture, and processing corrections (Sect. 5.2). Taking account of the noise in all these corrections, their one sigma upper and lower errors are derived. SEDs are assumed to be flat (νf_ν = constant). Column 7 is the flux bias defined as a ratio of true flux over measured one. Corresponding one sigma upper and lower limits are derived from Fig. 6. Column 8 is the completeness of the detection derived with 0.2 dex bins in Fig. 4.

Name	RA (J2000)	Dec (J2000)	Δr (arcsec)	Noise (μJy/beam)	6.7 μm (μJy)	Flux bias	Completeness
0	13 12 15.8	+42 43 60	2.5	2.7	19^{+11}_{-9}	$0.77^{1.03}_{0.59}$	0.24
1	13 12 16.8	+42 44 21	1.9	1.7	19^{+8}_{-7}	$0.77^{1.01}_{0.61}$	0.56
2	13 12 17.4	+42 44 53	2.3	1.7	14^{+7}_{-6}	$0.77^{1.00}_{0.60}$	0.32
3	13 12 18.0	+42 43 45	1.1	1.4	50^{+13}_{-12}	$0.90^{1.06}_{0.74}$	0.98
4	13 12 18.1	+42 45 28	2.3	2.2	18^{+9}_{-8}	$0.75^{1.01}_{0.59}$	0.36
5	13 12 18.1	+42 46 15	2.6	4.9	35^{+19}_{-17}	$0.77^{1.03}_{0.60}$	0.24
6	13 12 18.4	+42 43 20	1.1	1.8	66^{+17}_{-16}	$0.91^{1.06}_{0.74}$	0.98
7	13 12 18.7	+42 42 48	2.3	8.2	66^{+34}_{-30}	$0.78^{1.02}_{0.61}$	0.33
8	13 12 19.5	+42 44 60	1.9	1.1	12^{+6}_{-5}	$0.78^{1.02}_{0.61}$	0.55
9	13 12 19.5	+42 45 37	1.5	1.5	25^{+8}_{-8}	$0.85^{1.04}_{0.67}$	0.86
10	13 12 20.0	+42 44 38	1.4	1.1	21^{+7}_{-7}	$0.84^{1.06}_{0.65}$	0.89
11	13 12 21.0	+42 44 33	1.5	1.1	19^{+6}_{-6}	$0.82^{1.01}_{0.65}$	0.85
12	13 12 21.3	+42 46 24	2.3	7.9	63^{+32}_{-28}	$0.77^{1.00}_{0.60}$	0.32
13	13 12 21.4	+42 44 24	1.4	1.1	24^{+7}_{-7}	$0.87^{1.06}_{0.68}$	0.92
14	13 12 21.6	+42 44 05	1.5	1.1	19^{+7}_{-6}	$0.82^{1.03}_{0.64}$	0.88
15	13 12 21.6	+42 45 19	1.0	1.2	60^{+13}_{-14}	$0.94^{1.06}_{0.78}$	1.00
16	13 12 21.8	+42 43 48	1.5	1.1	19^{+6}_{-6}	$0.84^{1.03}_{0.67}$	0.86
17	13 12 22.6	+42 44 51	1.5	1.1	17^{+6}_{-6}	$0.84^{1.07}_{0.64}$	0.80
18	13 12 22.8	+42 43 15	2.7	1.2	8^{+5}_{-4}	$0.75^{0.98}_{0.60}$	0.17
19	13 12 23.1	+42 46 07	2.2	1.9	17^{+9}_{-7}	$0.79^{1.07}_{0.59}$	0.42
20	13 12 23.4	+42 45 17	1.5	1.1	20^{+7}_{-6}	$0.82^{1.02}_{0.65}$	0.87
21	13 12 23.4	+42 44 31	2.3	1.1	9^{+4}_{-4}	$0.78^{1.00}_{0.61}$	0.34
22	13 12 24.0	+42 45 43	0.9	1.4	135^{+24}_{-22}	$0.97^{1.04}_{0.90}$	1.00
23	13 12 24.3	+42 43 59	2.3	1.1	9^{+4}_{-4}	$0.76^{0.98}_{0.61}$	0.33
24	13 12 24.5	+42 43 23	2.0	1.1	12^{+5}_{-5}	$0.77^{1.01}_{0.59}$	0.50
25	13 12 24.7	+42 44 15	1.1	1.1	39^{+10}_{-9}	$0.90^{1.05}_{0.75}$	0.98
26	13 12 24.8	+42 45 10	2.1	1.1	10^{+5}_{-4}	$0.76^{1.02}_{0.59}$	0.44
27	13 12 25.2	+42 46 00	1.2	1.4	45^{+12}_{-12}	$0.91^{1.07}_{0.74}$	0.97
28	13 12 25.3	+42 43 46	1.3	1.1	27^{+8}_{-8}	$0.85^{1.04}_{0.66}$	0.95
29	13 12 25.7	+42 43 19	2.4	1.1	8^{+5}_{-4}	$0.77^{1.04}_{0.60}$	0.27

(Hughes et al. 1998). Our map also has a high source density, but 1/30 sources per beam. We suggest that the deviation from the theoretical prediction is related to the high source density and also to the finite pixel size (dotted line) at high *S/N*.

4.2.3. Flux errors and biases

Flux measurements always have errors. This effect can be well understood using the plot of assigned and measured fluxes normalized by their noise values in Fig. 6. In this plot of input and output *S/N*s, we draw the unity line (dashed line) and one sigma deviation lines both for the positive and negative sides (dotted lines). The distribution of the simulation results on this plot is fairly well represented by these two dotted lines. Here we show simple moving averages and their associated one sigma errors calculated from Eq. (A.2) using solid circles with vertical error bars. Large positive deviations from the unity line at low assigned *S/N*s are mainly due to the incompleteness

Table 3. continued.

Name	RA	Dec	Δr	Noise	6.7 μm	Flux bias	Completeness
	(J2000)		(arcsec)	(μJy/beam)	(μJy)		
30	13 12 26.2	+42 42 27	1.6	4.9	70^{+28}_{-25}	$0.82^{1.06}_{0.63}$	0.75
31	13 12 26.3	+42 45 26	3.2	1.1	6^{+3}_{-3}	$0.72^{0.86}_{0.59}$	0.08
32	13 12 26.3	+42 44 06	2.1	1.0	9^{+5}_{-4}	$0.78^{1.06}_{0.59}$	0.43
33	13 12 27.4	+42 44 49	1.5	1.1	17^{+6}_{-6}	$0.84^{1.07}_{0.65}$	0.82
34	13 12 27.7	+42 46 32	2.4	5.9	45^{+23}_{-21}	$0.76^{0.98}_{0.59}$	0.30
35	13 12 27.7	+42 45 35	1.7	1.1	15^{+6}_{-5}	$0.80^{1.03}_{0.62}$	0.71
36	13 12 27.7	+42 45 09	2.4	1.1	8^{+4}_{-4}	$0.76^{1.02}_{0.59}$	0.27
37	13 12 27.9	+42 42 20	2.4	11.8	87^{+45}_{-40}	$0.74^{0.97}_{0.58}$	0.27
38	13 12 28.3	+42 44 30	2.1	1.0	10^{+5}_{-4}	$0.75^{1.01}_{0.59}$	0.45
39	13 12 28.5	+42 46 02	1.5	1.7	27^{+10}_{-9}	$0.86^{1.08}_{0.68}$	0.83
40	13 12 28.5	+42 44 52	1.7	1.1	14^{+6}_{-5}	$0.80^{1.02}_{0.62}$	0.70
41	13 12 28.6	+42 43 60	1.1	1.1	46^{+10}_{-10}	$0.93^{1.05}_{0.78}$	0.99
42	13 12 28.9	+42 46 19	2.3	3.8	32^{+17}_{-14}	$0.78^{1.04}_{0.60}$	0.37
43	13 12 29.0	+42 43 07	2.1	1.2	12^{+6}_{-5}	$0.75^{1.01}_{0.59}$	0.46
44	13 12 29.2	+42 45 59	1.3	1.6	37^{+12}_{-11}	$0.84^{1.03}_{0.65}$	0.95
45	13 12 29.4	+42 44 40	3.0	1.1	7^{+4}_{-3}	$0.74^{0.92}_{0.61}$	0.12
46	13 12 29.6	+42 43 01	2.3	1.3	11^{+6}_{-5}	$0.75^{1.00}_{0.59}$	0.36
47	13 12 29.9	+42 44 08	1.5	1.0	16^{+6}_{-5}	$0.84^{1.07}_{0.64}$	0.80
48	13 12 29.9	+42 45 14	2.3	1.1	9^{+5}_{-4}	$0.77^{1.02}_{0.61}$	0.37
49	13 12 30.0	+42 44 20	1.6	1.0	15^{+6}_{-5}	$0.82^{1.05}_{0.63}$	0.75
50	13 12 30.1	+42 44 59	1.5	1.1	19^{+6}_{-6}	$0.85^{1.04}_{0.67}$	0.86
51	13 12 31.1	+42 43 33	1.4	1.1	22^{+8}_{-7}	$0.84^{1.06}_{0.64}$	0.91
52	13 12 31.5	+42 42 44	2.3	3.0	24^{+12}_{-10}	$0.75^{0.99}_{0.59}$	0.36
53	13 12 31.5	+42 42 36	2.9	4.3	27^{+15}_{-14}	$0.74^{0.94}_{0.60}$	0.11
54	13 12 31.6	+42 45 51	0.9	2.1	167^{+32}_{-35}	$0.95^{1.05}_{0.81}$	1.00
55	13 12 31.8	+42 43 48	1.9	1.0	12^{+5}_{-4}	$0.75^{0.98}_{0.59}$	0.58
56	13 12 32.0	+42 45 05	2.4	1.1	8^{+4}_{-4}	$0.74^{0.97}_{0.58}$	0.27
57	13 12 32.0	+42 44 32	1.5	1.0	18^{+6}_{-6}	$0.83^{1.02}_{0.66}$	0.88
58	13 12 32.9	+42 43 11	2.6	2.0	15^{+8}_{-7}	$0.76^{1.02}_{0.60}$	0.24
59	13 12 34.0	+42 44 42	1.6	1.3	18^{+7}_{-6}	$0.80^{1.03}_{0.62}$	0.74
60	13 12 34.2	+42 46 02	3.3	4.4	26^{+16}_{-14}	$0.72^{0.97}_{0.58}$	0.07
61	13 12 34.5	+42 43 41	1.3	2.3	55^{+16}_{-16}	$0.85^{1.03}_{0.66}$	0.95
62	13 12 34.7	+42 43 08	1.8	7.1	88^{+36}_{-31}	$0.80^{1.03}_{0.63}$	0.66
63	13 12 35.0	+42 45 05	2.1	1.9	18^{+9}_{-7}	$0.76^{1.01}_{0.59}$	0.48
64	13 12 35.8	+42 43 60	1.3	4.7	107^{+34}_{-33}	$0.85^{1.06}_{0.65}$	0.94

of detections. Almost no sources are detected with measured fluxes less than two sigma. Even at relatively high *S/N*s, there are slight positive deviations from the unity line. This could be due to effects of source confusion.

It should be noted that this simple relation from input *S/N*s to output *S/N*s cannot be applied in the opposite direction: from measured fluxes to their true fluxes. In this case one must take into account the probability distribution of detected sources over this plot. Such a distribution can be derived by convolving the simulation results on this plot with the probability distribution along the horizontal axis (true sources), i.e., differential number counts, and also the completeness of detection (Fig. 4).

For the convolution calculation, we introduced fine 0.03 dex meshes over the plot in accord with the steep slope of the number counts (Sect. 6.1). All we needed here was relative weights of the meshes along the horizontal axis at each vertical position. We assumed that the number counts were expressed with a single power. In this case, the relative weights were determined by relative flux levels. Thus, we could use the *S/N* horizontal axis. We then applied the completeness values to these weights. Convolving the final weights with the simulation

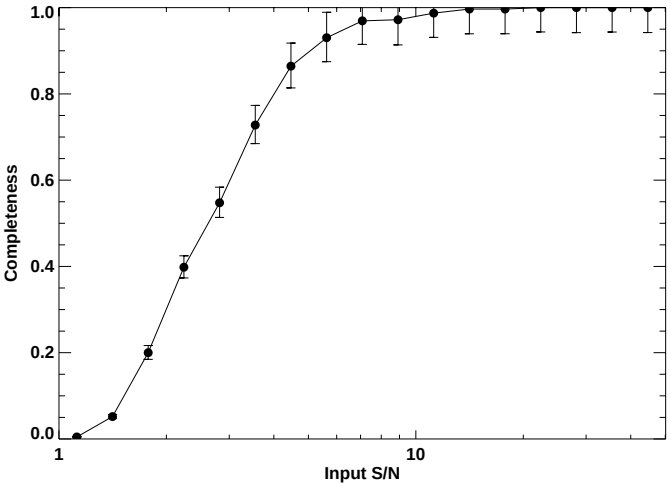

Fig. 4. The completeness of the detection as a function of input *S/N* (Sect. 4.2.1). A single test source was added to the *S/N* map (Fig. 2) to evaluate the completeness of the detection procedure. Almost 50 000 sets of *S/N*s and positions were used. One sigma errors were estimated assuming Poisson statistics (Gehrels 1986).

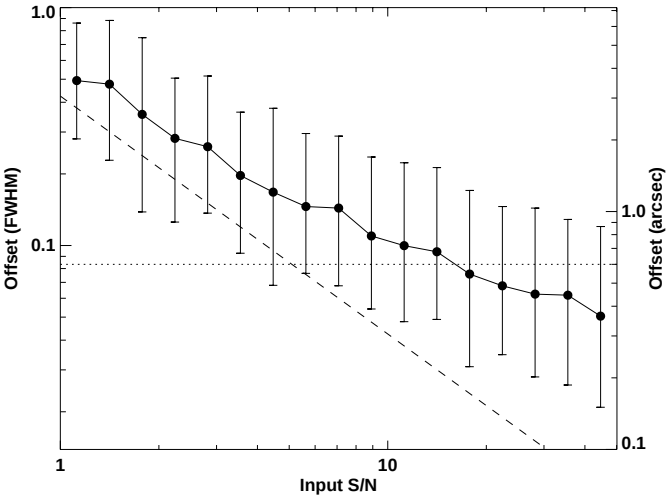

Fig. 5. The offsets of the output coordinates from the input ones. They are shown as a function of assigned *S/N*s of the test sources. One sigma errors were estimated with Eq. (A.2). Upper and lower sigma values were derived separately. The dashed line denotes the statistical formula for positional errors $\sigma_{\rm pos} = FWHM/\sqrt{8\ln 2}/(S/N)$ (Condon 1997). The size of sub-pixels in our map (0.6 arcsec) is also shown (dotted line).

results, the transformation from measured *S/N*s to statistically true *S/N*s was derived and is shown as the red solid circles with horizontal error bars in Fig. 6. Note that the assumed power of the differential number counts should be derived only after the correction of this flux bias. Thus, some iterations were needed here.

Since the noises for the input and output *S/N*s are measured on the noise map and are thus irrelevant to the simulations, this gives the relation between input and output fluxes. Because the slope in number counts is negative, fainter sources (less significant sources in this plot) are more numerous. As a result, the true flux bias (red circles) is larger than the simple relation

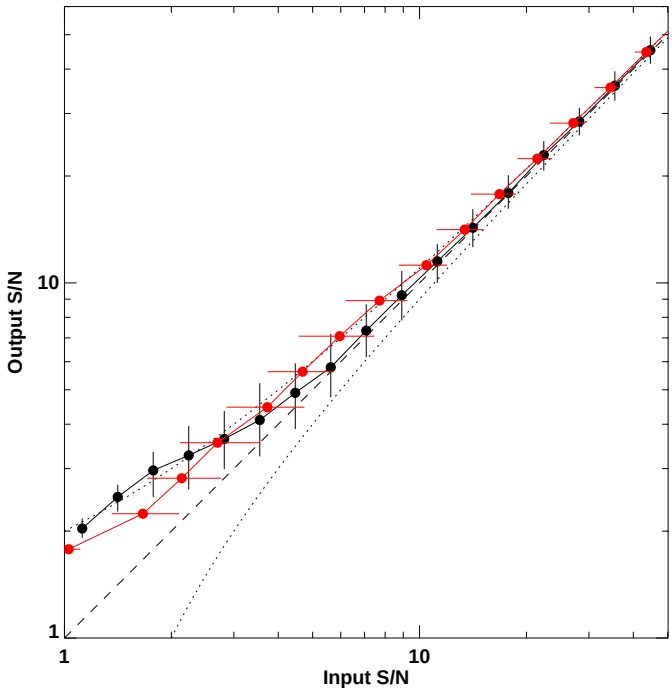

Fig. 6. The output *S/N* of the detected source as a function of input *S/N*. The individual simulation results are distributed almost within the nominal one sigma limits (dotted lines) along the unity line (dashed line). Due to a combined effect of the incompleteness and the source confusion, the distribution is biased toward higher output *S/N*s. Means of the distribution and their one sigma errors are shown with solid circles with vertical error bars. For the correction of this flux biasing effect in the direction from output to input, the probability distribution over the diagram should be considered (Sect. 4.2.3). It can be derived by convolving the simulation results with the differential number counts and their completeness along the input *S/N* axis. The resulting relation from output *S/N*s to input *S/N*s is presented with the red solid circles with horizontal error bars. (This figure is available in color in electronic form.)

(black circles) where the completeness is almost maintained. Beyond the point where the completeness begins to steeply decline to zero at the low input *S/N*s or faint fluxes, the large deviations from the unity line seen in the simple relation begin to be suppressed.

Flux biases for the detected sources are listed in Table 3; however, this correction is highly statistical. For example, if a particular source is known to be isolated, the correction derived here would be somewhat overestimated since the effect of source confusion would be smaller for that source.

5. The catalog

Table 3 lists the properties of all the 65 sources detected with the detection parameters described in Sect. 4.1. Here we explain the absolute calibration of the coordinates and the fluxes.

5.1. Astrometry – coordinates

The coordinates in the catalog were calibrated with the USNO A2.0 catalog (Monet et al. 1998) extracted at the VizieR database (Ochsenbein 1997). Because very few *LW*2 sources

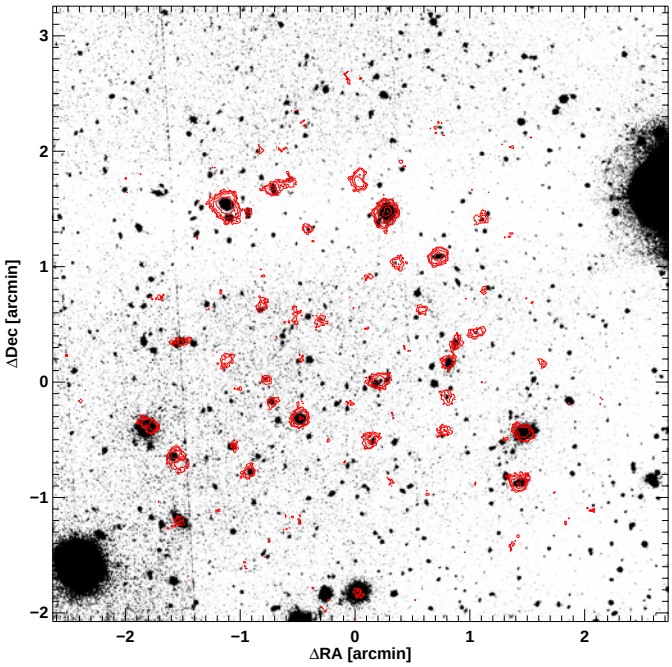

Fig. 7. *LW*2 *S/N* contours superimposed on the *I* band image. The image registration is performed using the astrometric solution obtained in Sect. 5.1. The contour levels are set to 3, 4, 6, 10 and 18 sigmas in sub-pixels (Fig. 2). (This figure is available in color in electronic form.)

were identified in the USNO catalog, the calibration was performed in two steps. The USNO catalog was first used to establish the coordinate system in the *I* band image that was taken from the ground (Cowie et al. 1996). The astrometric solution with 7 sources in the *I* band image shows a mean deviation of 0.″25. The *I* band image was then compared with the *LW*2 image. Excluding confused sources, 12 sources in the *LW*2 band were used to derive the astrometric solution, giving a mean deviation of 0.″75. Then the absolute astrometric error of the coordinate system in the *LW*2 image is 0.″79. The major cause of this error is the combined effect of the significant undersampling of the instrumental beam with 6 arcsec pixels and the transients in the *LW* array (Sect. 5.2). The total astrometric error for an individual source is calculated as a quadratic sum of the absolute astrometric error and the relative astrometric error determined with Fig. 5. For sources with high completeness, this total astrometric error is conservative, because the effects of finite pixels have been accounted for twice.

Figure 7 shows the *LW*2 *S/N* contours superimposed on the *I* band image with the astrometric solution derived above. Many bright *I* band sources are easily identified with *LW*2 sources. We counted numbers of bright ($I < 23.7$) sources for high and low completeness *LW*2 samples; there are 35 *LW*2 sources with completeness larger than 0.5 and 30 sources with lesser completeness. Within a distance of 1.5 times the total astrometric error from the measured coordinates, 28 and 24 *I* band sources were found. The surface density of $I < 23.7$ sources suggests that there would be 0.51 and 1.2 chance associations in the searched areas. Subtraction of these numbers gives rates of finding $I < 23.7$ sources as 79 and 76% for the high and low completeness samples respectively. This small decrease in the rate indicates the high reliability of the catalog even for sources with low completeness.

5.2. Photometry – flux

The flux in the catalog is calculated statistically to be a total flux for a single point-like source. The total flux $F_{\rm total}$ is obtained with the formula $F_{\rm total} = F_{\rm beam} \times 2.0 / 0.52$. For each detected position, an aperture flux with 7.2 arcsec diameter is measured in units of ADU/G/s on the signal map. This flux is corrected using the flux bias determined in Sect. 4.2.3. This gives $F_{\rm beam}$. The two factors, 2.0 and 0.52, represent aperture and processing corrections which will be explained below. The $F_{\rm total}$ in units of ADU/G/s is then converted with a sensitivity parameter 2.32 ADU/G/s/mJy (Blommaert 1998).

The aperture correction was determined using the real data. Growth curves of the detected sources become noisy at diameters larger than 18 arcsec, but the dispersion was almost a minimum at 7.2 arcsec. Thus, the aperture correction from a 7.2 arcsec flux to an 18 arcsec flux was adopted. Similar to 7.2 arcsec flux measurements (Sect. 4.2.3), there would be flux biases in 18 arcsec flux measurements. We therefore performed simulations for the 18 arcsec measurements similar to those for the 7.2 arcsec measurements, and corrected the flux bias in the 18 arcsec measurements. The aperture correction factors were then obtained using the bias corrected 7.2 and 18 arcsec flux measurements for the 8 brightest sources, which resulted in a median of 2.0 with a one sigma error of 9.8% (Eq. (A.2)). At this stage, bias-corrected 18 arcsec fluxes were derived.

Next, the processing correction factor was derived simulating all the image processing steps by independent simulations different from those in Sect. 4.2. This processing correction is needed not only to translate the bias-corrected 18 arcsec fluxes to total ones but also to assess any effects in the image processing. Such processing effects are usually canceled out by a comparison with observational data for external calibration sources that have been processed in the same manner. However, in this case no such data exist due to the specification of the ISOCAM observations.

We therefore explain here the simulations used to derive the processing correction factor. At first, we needed to prepare simulated raw data. A total flux was assigned to a simulated source using the sensitivity parameter, and the source was put at a random position on the sky with the theoretical point spread function (PSF; Okumura 1998). It was then reprojected on the *LW* array at every exposure position using the satellite coordinates at every time step and the measured offsets among revolutions. The optical distortion coefficients of the *LW* array (Aussel 1998) were also taken into account. The derived source signals were modified with the formula of the transient (Eq. (6) in Coulais & Abergel 2000) using the measured background flux (cf. Fig. 8). Then, the measured responsivity drifts and dark signals based on the dark model were applied. Finally, we added the real ISOCAM raw data to these simulated raw data to simulate noise. This approach was mandatory because

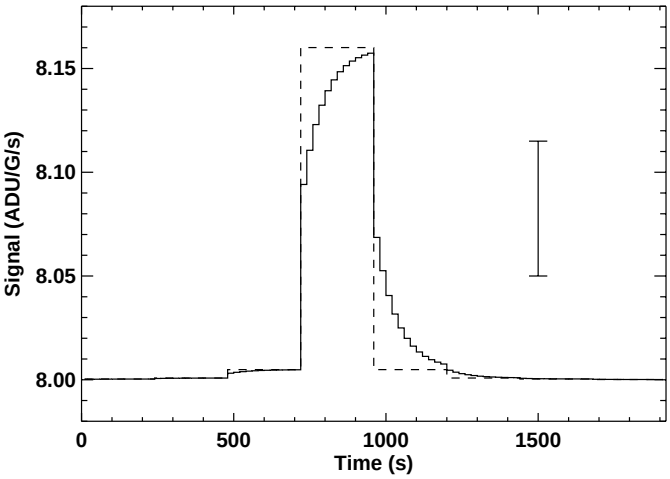

Fig. 8. An example of the transient effect of the ISOCAM *LW* array. The dashed line denotes the signal from an ideal detector free from the transient effect. A point source is assumed to pass over the center of the pixel with raster movement having a step size of 7 arcsec. The solid line represents the expected signal with the transient formula by Coulais & Abergel (2000). This figure assumes an instantaneous response of $\beta = 0.51$, a time constant of $\lambda = 560$ ADU/G, a background flux of 8 ADU/G/s, and a source flux of 100 μJy. The vertical bar in the panel is a typical one sigma noise for each exposure. This implies that the transient correction for faint sources would only be performed statistically on the final product.

the noise properties in the ISOCAM data had not been properly understood.

Next we applied the same image processing steps to these simulated raw data. The PSFs of simulated sources on the final map were found to be almost one arcsec sharper than those of real sources. This suggests that the technique for making simulated raw data was not perfect. One of the reasons for the sharper PSFs of the simulated sources could be errors in the measured offsets among revolutions. If the measured offsets were different from real values, PSFs of real sources would become broader artificially, while such effects cannot be involved in simulated sources. Actually, the magnitude of the differences in PSF widths is almost comparable to the total astrometric errors measured for real sources. There could be other possibilities such as errors in the optical distortion coefficients, theoretical PSFs which are too sharp, and ignoring cross-talk in the transient formula.

In any case, the effects on the correction factor to the total flux due to this discrepancy in the PSF shape will be minimized for the large 18 arcsec aperture. We found that the bias-corrected 18 arcsec fluxes for the simulated sources corresponded to $52^{+6.1}_{-4.7}$% of their total fluxes. There was no meaningful correlation between the correction factor and the input flux level. One of the main reasons for the large deviation from 100% may be our technique for responsivity correction. In this process, non-stabilized source signals are divided by responsivities which are too high due to transient remnants (cf. Fig. 8).

6. Number counts at 6.7 μm

6.1. Galaxy number counts

To derive galaxy counts, we have to identify stars in the catalog. We adopted SExtractor stellarity indices (Bertin & Arnouts 1996) measured with the ground-based *B* and *I* band images (cf. Fig. 7). The stellarity indices were calibrated with the *HST I* band image having a partial coverage of the field (Cowie et al. 1995a). Two bright (>100 μJy) *LW*2 sources, #22 and #64 in the catalog, were then categorized as stars based on their high stellarity indices. At galactic latitude $|b| = 50°$, Franceschini et al. (1991) estimated that galaxies should dominate the 6.7 μm source counts below 90 μJy. At this flux level, star counts should be 0.15 arcmin^{-2}, which is similar to our result of two stars in our survey area (16 arcmin^2). In the following discussion, all the sources in the catalog are assumed to be galaxies except #22 and #64.

The number count is the number of sources in an unit solid angle with a certain flux constraint. It can be obtained from an observation as a sum of inverse of maximum solid angles in which the sources could be detected;

$$N(S) = \sum_i \left(\frac{1}{\Omega_i}\right), \tag{12}$$

where $N(S)$ denotes a differential number count in a flux bin at flux S, i is a running number for detected sources in the corresponding flux bin, Ω_i is a maximum solid angle having a sensitivity to detect the source i. Integral number counts $N(>S)$ will be obtained by summing up $N(S)$. In order to avoid unwanted effects due to negative sources, we restrict the summation to the significance level that could exclude negative sources. This level corresponds to a completeness of 56%. Then the least significant source in the summation has a *S/N* of 4.3 in the map coaddition.

Any incompleteness requires a calculation of effective solid angles. As the noise level is not uniform in our map, the effective solid angle Ω should be obtained as an integral;

$$\Omega(>S) = \int \gamma(S/N)\mathrm{d}\Omega(N), \tag{13}$$

where γ denotes a completeness as a function of S/N. The map is divided into small pieces $\mathrm{d}\Omega(N)$ giving the same noise level N. We convolve the non-uniform noise map with a 7.2 arcsec diameter aperture and relate them with the photometry of the detected sources using the aperture and processing correction factors (Sect. 5.2). To go well with the restriction of the summation, γ is set to zero for $\gamma < 0.56$. The derived effective solid angles $\Omega(>S)$ are shown in Fig. 9 as a function of flux.

Then, integral galaxy number counts $N(>S)$ at 6.7 μm are obtained as listed in Table 4. The integral number counts climb up to 1.3×10^4 deg^{-2} at the faintest limit. The counts can be approximated with a single power -1.6 between 13 μJy and 130 μJy as

$$N(>S) = 2.1^{+0.5}_{-0.4} \times 10^3\ [\mathrm{deg}^{-2}] \left(\frac{S}{40\ [\mu\mathrm{Jy}]}\right)^{-1.6\pm0.3}. \tag{14}$$

Table 4. The galaxy number counts at 6.7 μm. $N(>S)$ are integral counts and $N(S) = \Delta N(>S)/\Delta \log S$ are differential counts. $N_{\rm pos}(>S)$ shows a number of the detected sources with a flux larger than S, excluding the two stars. $N_{\rm neg}(>S)$ is a number of the detected sources in the negative map. $N_{\rm pos}(S)$ and $N_{\rm neg}(S)$ are numbers of the detected sources in the corresponding flux bins.

$\log S$ log (μJy)	S (μJy)	$N_{\rm pos}(>S)$	$N_{\rm pos}(S)$	$N_{\rm neg}(>S)$	$N_{\rm neg}(S)$	$N(>S)$ (deg^{-2})	$N(S)$ (deg^{-2})
2.3	200	0		0		0.0	
2.2	160		1		0		2.4×10^2
2.1	130	1		0		2.4×10^2	
2.0	100		1		0		2.6×10^2
1.9	79	2		0		5.1×10^2	
1.8	63		4		0		1.1×10^3
1.7	50	6		0		1.6×10^3	
1.6	40		5		0		1.6×10^3
1.5	32	11		0		3.2×10^3	
1.4	25		7		0		2.9×10^3
1.3	20	18		0		6.1×10^3	
1.2	16		12		0		6.9×10^3
1.1	13	30		0		1.3×10^4	

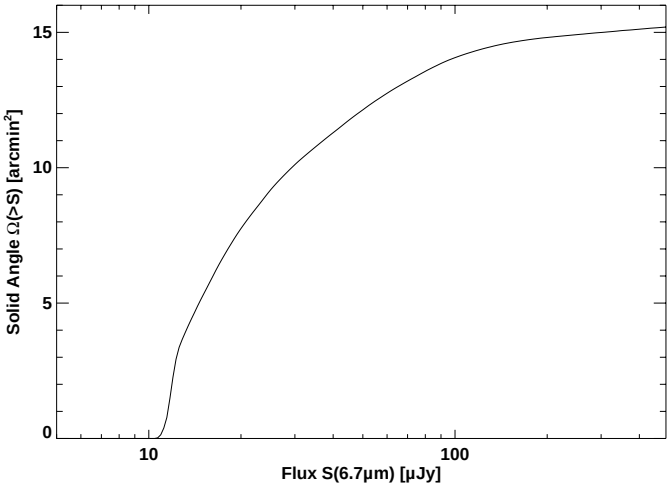

Fig. 9. Survey solid angles as a function of 6.7 μm flux. Completeness of the detection is taken into account down to 56%. Below this limit, the completeness is set to zero.

As the integral counts are not independent of each other, we also list the differential galaxy number counts $N(S)$ at 6.7 μm in Table 4.

The integral galaxy number counts are shown in Fig. 10 with error bars. The vertical bars are derived with the Poisson statistics (Gehrels 1986). The horizontal bars were obtained applying mean logarithmic flux error factors for the detected sources counted in those flux bins. The error ranges in flux becomes larger at fainter flux bins.

6.2. Extragalactic background light

Extragalactic background light (EBL) due to resolved galaxies can be derived as a first moment of the number counts:

$$\nu I_\nu(S) = c/6.7\,\mu{\rm m} \times \sum_i \left(\frac{S_i}{\Omega_i}\right), \quad (15)$$

where $\nu I_\nu(S)$ is the 6.7 μm EBL, S_i is the 6.7 μm flux of the source i, and c is the speed of light. Integrating the extragalactic contributions in the flux range of $\log S = 1.1{-}2.3$ for our counts (Table 4), we obtain the integrated 6.7 μm light of $0.56^{+0.12}_{-0.10}$ nW m^{-2} sr^{-1}. The upper and lower errors are derived as in Sect. 6.1. It should be noted that this integrated light is still a lower limit to the 6.7 μm EBL, because the slope of the number counts is steeper than -1 even at the faint bins. So the 6.7 μm EBL would become larger when integration to fainter flux levels becomes possible.

Recently, TeV γ-ray data were used to put constraints on the EBL in the infrared. This is based on electron-positron pair creation by photon collisions $\gamma_{\rm TeV} + \gamma_{\rm IR} \rightarrow {\rm e}^+ + {\rm e}^-$. Upper limit values on the infrared EBL are known to be sensitive to the assumed shape of the infrared EBL. If the infrared EBL had a local minimum around 5 μm, the 5 σ upper limit could become as low as 2 nW m^{-2} sr^{-1} (Renault et al. 2001). With a wide range of reasonable assumptions on the infrared EBL, a strict upper limit of 4.7 nW m^{-2} sr^{-1} between 5 and 15 μm was derived so far. From the galaxy modeling side, a value of 2.4 nW m^{-2} sr^{-1} at 6.7 μm was predicted with the assumed redshift of galaxy formation $z_{\rm F} = 9$ (Franceschini et al. 1991). Much more precise values of the EBL in this spectral range would put a strong constraint on the major epoch of star formation in galaxies (Primack et al. 1999).

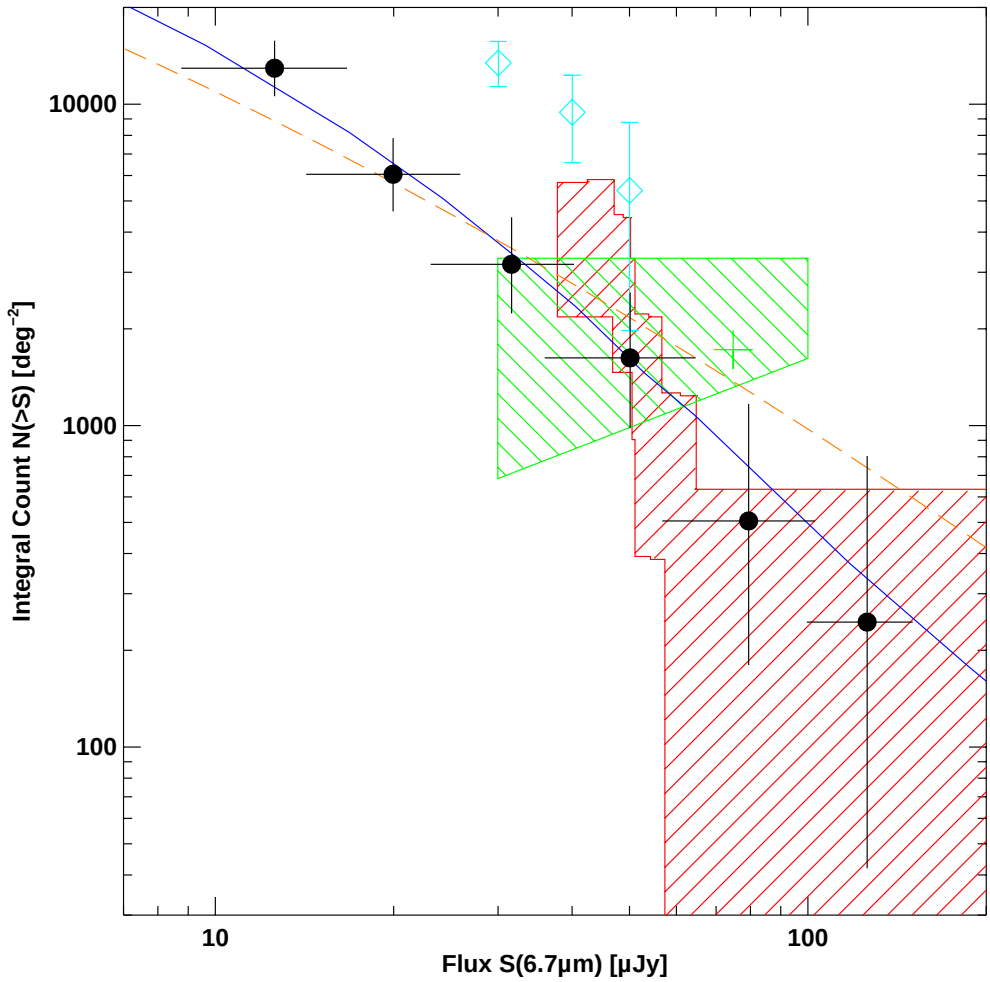

Fig. 10. The integral galaxy number counts at 6.7 μm. Our counts in the SSA13 field are marked with black filled circles with corresponding error bars (Sect. 6.1). The initial results and the re-evaluation of the HDF data are shown as red hatches (Oliver et al. 1997) and green hatches and a cross (Aussel et al. 1999). The counts for field galaxies through the cluster gravitational lens A2390 are marked as cyan diamonds with their error bars (Altieri et al. 1999). Model predictions are overlaid for two models. The blue line represents the Franceschini et al. (1997) model and the dashed orange line is the Rowan-Robinson (2001) model. (This figure is available in color in electronic form.)

6.3. Comparison with other 6.7 μm counts

Our counts go somewhat deeper than previously reported counts at 6.7 μm (Fig. 10). In the overlapping flux range, our 6.7 μm galaxy counts are almost consistent with the HDF counts (Oliver et al. 1997; Aussel et al. 1999). While the recent HDF-S counts (Oliver et al. 2002, not shown) are somewhat larger than the HDF and our counts, the field galaxy counts lensed by the massive cluster A2390 (Altieri et al. 1999) are about four times larger than ours.

The excess in the A2390 counts might be due to a failure in identification of cluster members. There may be errors in gravitational lensing corrections in flux and solid angle. Multiple lensed images might be counted as individual field galaxies. These effects could become more significant since the target field is at the center of the cluster and the surveyed area is more than two times smaller than ours. Another reason might be contamination by stars. The SSA13 field and the HDFs are located at high galactic latitudes: $b \sim 74°$ (SSA13), $b \sim 55°$ (HDF), and $b \sim -49°$ (HDF-S). A2390 is located at low galactic latitude ($b \sim -28°$). At $|b| = 20°$, stars are expected to dominate the counts even at a faint flux level of 3 μJy (Franceschini et al. 1991). Altieri et al. (1999) stated that only two stars were identified among their 31 detections. The solid angles of the Altieri et al. (1999) counts might be underestimated by subtraction of the pixel areas occupied with brighter sources. Aussel et al. (1999) did this and the nominal Aussel et al. (1999) count (green cross) is larger than the Oliver et al. (1997) counts in the HDF.

6.4. Comparison with models

There are essentially two approaches to predict galaxy number counts. One is a parametric evolution approach, which has been applied to IRAS 60 μm galaxy counts using IRAS 60 μm local luminosity function and its population mix. Normal spirals, starbursts, and AGNs are assumed to have non-evolving empirically determined SEDs but a parametric evolution in luminosity and/or density. After the observations with ISO and

SCUBA, many authors have extended this modeling mainly to explain ISO 15 μm counts and SCUBA 850 μm counts (Xu et al. 2003 and references therein). Some groups predict galaxy counts at 6.7 μm as well. Here we show the Rowan-Robinson (2001) model (dashed orange line in Fig. 10), which could be marginally consistent with our counts. This model is known to represent well bright 6.7 μm counts. This will be due to the following facts. In the local universe, the observing band of the ISOCAM *LW*2 (5–8.5 μm) filter matches the location of PAH and hot dust emission, which could be strong in star forming galaxies. Such low-redshift star-forming galaxies are known to be traced in the far-infrared, such as in the IRAS 60 μm band.

Another approach is a stellar population synthesis method, which is used to model optical and near-infrared galaxy counts in searches for cosmological parameters. E/S0 and spiral galaxies are assumed and their local luminosity functions are adopted in the optical or near-infrared. Their SEDs evolve with time as their stellar populations do. Some include an AGN contribution as a parametric evolution population. Franceschini et al. (1997) used this approach to model 6.7 μm counts (blue line in Fig. 10). Although the observational counts are associated with large errors, the consistency between this Franceschini et al. (1997) model and our results is remarkable. The steep slope comes from stellar emission of high redshift ($z > 1$) E/S0 galaxies. At this redshift, the ISOCAM *LW*2 band will start to select near-infrared emission from stellar photospheres in galaxies, especially in E/S0 galaxies which are assumed to have formed most of their stars in the early epochs. Moreover, stellar SEDs short-ward of 6.7 μm are steep up to 1 μm and their brightening at high redshifts is also expected. Because E/S0 galaxies lack PAH and dust emission in the local universe, there is a negligible contribution from E/S0 galaxies in bright 6.7 μm counts. This affects additional contributions from E/S0 galaxies in this faint flux range. In contrast with its good agreement with the faint 6.7 μm counts, the Franceschini et al. (1997) model is known to underpredict bright 6.7 μm counts, probably due to insufficient evolution of dusty galaxies in the stellar population synthesis method.

In this respect, a trial to combine these two approaches has been made by Xu et al. (2003). After constructing three parametric evolution models, each of which is consistent with existing dusty galaxy counts, they added E/S0 galaxy counts to each of them. The resulting counts have a slope consistent with our counts, but the counts themselves are much higher than ours, and in fact are more consistent with the A2390 counts. We think that their population of starbursts should be merged with E/S0 galaxies at high redshifts. Xu et al. (2003) themselves report a synchronization of active evolutionary phases of E/S0s and starbursts at high redshifts ($z > 1$). A method of stellar population synthesis has now been extended to the far-infrared, and it shows that SEDs of E/S0 galaxies can resemble those of starbursts in their early evolutionary phases (Silva et al. 1998). Interestingly, Pearson (2001) predicts excessive 6.7 μm counts similar to those of Xu et al. (2003) by adding a ULIG component to his parametric evolution model instead of an E/S0 component.

On the observational side, we find all submillimeter sources in the SSA13 field have SEDs consistent with high redshift ($z > 1$) galaxies having stellar masses comparable to those of typical E/S0s (Sato et al. 2002). At the shorter wavelengths, a deficiency of high redshift ($z > 1$) elliptical galaxies was reported from optical observations with spectroscopic and photometric redshifts (Franceschini et al. 1998). The number of morphologically identified elliptical galaxies at faint magnitudes ($I > 24$) was found to be smaller than the model predictions (Driver et al. 1998). Instead, the number of disturbed faint galaxies was reported to be larger and some of them were identified with high redshift galaxies (Cowie et al. 1995a,b). All these support the idea that elliptical galaxies undergo dusty starbursts at high redshifts. However, similar number count predictions can be reproduced with a different set of SEDs and evolutionary parameters, especially in a parametric evolution approach as shown in the three parametric evolution models presented by Xu et al. (2003). Thus, a definite answer must await detailed investigations of individual faint 6.7 μm galaxies detected in this survey (Sato et al. 2003).

7. Summary

A very deep mid-infrared survey has been conducted to investigate evolution of field galaxies at high redshift. The high galactic and high ecliptic latitude field SSA13 has been imaged with the ISOCAM's broad band filter at 6.7 μm.

Utilizing quite high redundancy with a total observing time of 23 h, we have developed a correction for responsivity drifts. We also introduced several types of masking and median noise estimates for data affected by outliers (Appendix A). Many simulations have been carried out to properly account for the characteristics of the image processing and source detection. Within an area of 16 arcmin^2, 65 mid-infrared sources down to 6 μJy have been detected. For the central 7 arcmin^2, an 80% completeness limit reaches 16 μJy.

The galaxy number counts have been derived with statistical corrections. The slope of the integral counts is -1.6 between 13 μJy and 130 μJy and the counts exceed 1×10^4 deg^{-2} in the faint limit. Our counts reach a limit about three times fainter than those in the HDFs. Although more detailed investigations are necessary, the steepness of the counts might indicate that stellar emission of evolving E/S0 galaxies has redshifted into the ISOCAM *LW*2 bands at this faint level.

Acknowledgements. YS would like to thank Minoru Freund and Mikako Matsuura for their dedicated hardware provisions in the early phases. We have received many useful comments from Leo Metcalfe, the leader of ISOCAM Instrument Dedicated Team during the ISO operational phase. Leo Metcalfe and Bruno Altieri have suggested the cosmic ray deglitching based on the data pointing at the same sky position. Discussions with Shinki Oyabu were very useful. We are indebted to the first referee for the detailed suggestions during the long referring process and the second referee for complementary and constructive comments. The analysis has been achieved with the IDL Astronomy Users Library maintained by Wayne Landsman. This research has made use of NASA's Astrophysics Data System Bibliographic Services. A part of this research has been supported by JSPS Research Fellowships for Young Scientists.

Appendix A: Details of the image processing

The image processing is summarized in Sect. 3. Here we describe details of that processing; creation of *raw*, *dsub*, *sresp*, *ofrac*, and *obj* data, object masking, cosmic ray masking, and noise estimates with median absolute deviation. Map creation and noise investigation are also described.

A.1. Dark subtraction

Although all the processing steps in Sect. 3 are considered for one detector pixel, procedures in this subsection can be applied frame by frame. The raw signal frame *raw* in Eq. (1) was derived as a difference of ISOCAM image frames taken at the reset and the end of integration. Subtraction of the dark image frame *b* from the *raw* frame gave the dark-subtracted frame *dsub*. The dark image frames were created with the dark model invented and updated by Biviano et al. (1998) and Roman & Ott (1999).

A.2. Median absolute deviation as a noise estimator

The subsequent processing requires threshold values to identify objects and cosmic rays such as 3 sigma detection or 3 sigma rejection thresholds. In order to obtain such thresholds, one of the robust noise estimators – median absolute deviation – was adopted. Median absolute deviation τ is defined here as

$$\tau = \mathrm{med}(\mathrm{abs}(x_i - \mathrm{med}(x_i))) \quad \text{(A.1)}$$

for sample x_i. Detector noise, the sum of readout and photon noises, can be represented with the τ, because the median operations in Eq. (A.1) are insensitive to outliers such as cosmic rays. The τ was then scaled to give it the statistical meaning of the Gaussian sigma σ as

$$\sigma_\tau = \tau/\tau_0, \quad \text{(A.2)}$$

where $\tau_0 = 0.67448975$. The scaling factor τ_0 is the τ for a sample with a Gaussian distribution with $\sigma = 1$.

For the *dsub* data, σ_τ was calculated for each pixel in each revolution. With these σ_τ as starting values, all the error propagation was traced in the subsequent arithmetic operations.

A.3. Responsivity correction

A.3.1. Raster point masking

When we are looking at blank sky, detector signals are dominated by the zodiacal emission. The zodiacal emission depends on the solar aspect angle (Table 1). The temporal variation of the solar aspect angle is almost negligible during observations lasting less than several hours. Thus, the responsivity of the detector can be monitored by using blank sky as a reference.

Because the responsivity drifts are major noise sources, creating the response to sky *sresp* is the most essential part of the image processing. The *sresp* data were derived from the dark-subtracted data *dsub*. Because of the different sky levels among revolutions (Table 1), this operation was performed separately with the data taken in each individual revolution.

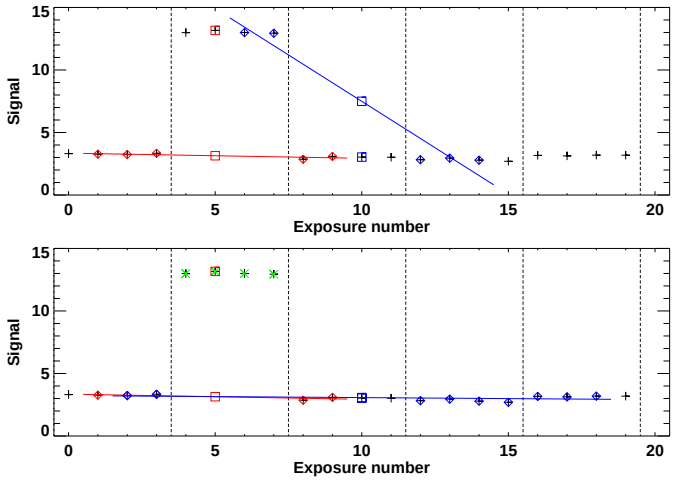

Fig. A.1. Schematic diagrams for the derivation of the response to the sky *sresp*. The top panel shows the derivation with raster point masking. The number of exposures per raster point is set to four (i.e. $N_{\mathrm{exp}} = 4$). Plus signs show dark-subtracted *dsub* signals of a detector pixel during five raster point observations. Vertical dotted lines show boundaries of raster points. A *sresp* value for exposure #5 (a red square on a red line) is derived with a line fitted to five *dsub* samples (red diamonds). In the bottom panel, object masks are applied. Four *dsub* samples at the second raster point are masked out (green asterisks). A *sresp* value for exposure #10 (a blue square on a blue line) is then derived correctly with a line fitted to nine unmasked *dsub* samples (blue diamonds). (This figure is available in color in electronic form.)

The top panel of Fig. A.1 shows a schematic diagram for the *sresp* creation. A *sresp* value is to be assigned to each exposure. This value is evaluated via a linear interpolation of four or more *dsub* samples in adjacent raster points. For example, a *sresp* value for exposure #5 (a red square on a red line) is derived by fitting a straight line to three *dsub* samples at the first raster point (#1, 2, and 3) and two *dsub* samples at the third raster point (#8 and 9). Similarly, a *sresp* value for exposure #6 will be derived from five *dsub* samples (#2, 3, 8, 9, and 10). Because no *dsub* samples in its own raster point is used to derive a *sresp* value, we call this technique *raster point masking*.

In the neighborhood of exposures with contributions from objects, however, the raster point masking gives higher *sresp* values than the correct ones. Such an example is shown for a *sresp* value for exposure #10 (a blue square on a blue line). In this setting, all the exposures at the second raster point should be masked out, because the detector is looking at a bright object at that raster point. With such masks, *sresp* values are then derived correctly. We will discuss such a procedure just after explaining object masks below.

A.3.2. Object masks

With the responsivity correction, division of the *dsub* data with the *sresp* data (Eq. (8)), and the subsequent normalization (Eq. (10)), the *obj* data were obtained. They were calibrated to have zero flux for the sky. Thus, any positive features should be objects. The estimated noise is around 30 μJy per pixel (1 σ) at this stage. Thus, almost no object could be identified in our *obj* data (Sect. 5.2).

A low noise map must be derived in order to determine the location of the objects. All the *obj* data taken in a single revolution are then coadded (Appendix A.6). The resulting map is called a *revolution map*. The noise found in the revolution map was more than ten times smaller due to coaddition of a few hundred *obj* data in a revolution. At this stage, many bright sources could be identified with a certain threshold. Note that median values were used in the coaddition to suppress contamination by cosmic rays.

The objects on the 2-dimensional (2-D) revolution map needed to be located in the 3-dimensional (3-D) data, because the *sresp* data are calculated with the 3-D *dsub* data. However, there is a complicated relation between sub-pixels in the 2-D revolution map and pixels in the 3-D data, due to raster slews, the optical distortion of ISOCAM and the use of sub-pixels in a revolution map (Appendix A.6). Thus, the projection of the 3-D *obj* data to the 2-D revolution map was reversed. The resulting 3-D data are called reversely-projected object *robj* data. Any pixel in the 3-D *robj* data can be compared with that in the 3-D *dsub* data. This transformation from 2-D to 3-D is designed so that *S/N* in the 3-D *robj* data is the same as in the 2-D revolution map. A single *S/N* threshold was then used to mask pixels in the 3-D data looking at objects.

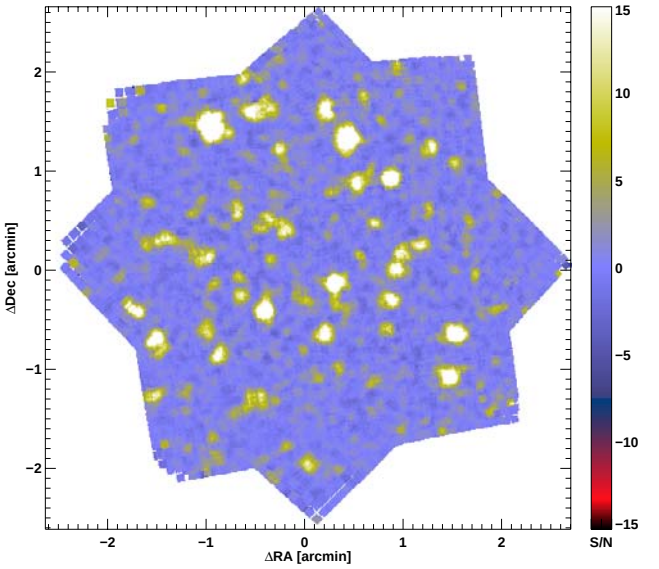

Fig. A.2. A trial map constructed as if the data were taken with $N_{\rm exp}$ = 1. The object masks were made from the final map (Fig. 2) with 2.5 sigma for the identification threshold parameter. For the display, the noises in sub-pixels are normalized to correct the noise correlation in the map creation stage. (This figure is available in color in electronic form.)

A.3.3. Raster point masking with object masks

Now, we could apply the object masks to the *dsub* data. The raster point masking (Appendix A.3.1) was then repeated on the object-masked *dsub* data to refine the *sresp* data.

The bottom panel of Fig. A.1 shows a schematic diagram for the raster point masking with object masks. All the *dsub* data samples at the second raster point are object-masked (green asterisks). A *sresp* value for exposure #10 (a blue square on a blue line) is then derived from nine *dsub* samples #2, 3, 12, 13, 14, 15, 16, 17, and 18 (blue diamonds). Note that a *sresp* value is estimated as the midpoint of the fitted line and at least two samples are required at one side of the fitted region to properly interpolate the responsivity drifts.

In order to avoid inadequate interpolation, pixel history was regarded as discontinuous at positions having more than 3 σ deviation from the previous data. Near the discontinuities, the conditions of linear interpolation above can not be satisfied. Any exposures for which *sresp* values could not be defined were not used for the subsequent processing (Fig. 1).

The raster point masking with object masks was repeated three times. The object identification thresholds were decreased; 5, 4, and 3 sigmas in this order. Note that no normalization of the noises in 6 arcsec pixels has been applied. At the final stage, the object masks occupy 3% of the data.

A.3.4. Dwelling time and timescale of the responsivity drifts

Some discussion is warranted concerning an appropriate value for the number of exposures per raster point; $N_{\rm exp}$ = 12 for our case. Suppose one pixel looked at an object at the *i*th raster point and it looked at sky at the adjacent raster points. The raster point masking routine calculates the *sresp* values for the *i*th raster point by interpolating the *dsub* data at the adjacent raster points. If the *dsub* data at the *i*th raster point are larger than the interpolated *sresp* data, this excess is recognized as an object. Because the responsivity is drifting, the noise caused in the interpolation becomes larger, if the time interval increases between the data at the *i*th raster point and the reference data at the adjacent raster points.

To evaluate this effect, a trial map was created with an assumption that the data were taken as if $N_{\rm exp}$ = 1 (Fig. A.2). The object masks were created from the final map (Fig. 2) with an object identification threshold of 2.5 sigma. As expected, fluctuation in the background became roughly four times smaller than that in the final map. This indicates that smaller $N_{\rm exp}$(<12) would be preferable to correct the responsivity drifts. Note that any objects below the identification threshold will never have appeared in this trial map.

A.4. Cosmic ray masks – deglitching

The *dsub* data contain many spikes (top panel of Fig. 1). Such spikes, usually called glitches, were caused by cosmic ray impacts on the detector pixels. Glitches are short term phenomena, lasting a couple of exposures, and thus differ from the long term responsivity drifts. The deglitching algorithm was developed to remove glitch effects in our data with $T_{\rm int}$ = 20 s. There are three masking steps based on *dsub*, *obj*, and *robj* data.

Suppose that a glitch lasts N exposures in the *dsub* data. To remove this glitch with a time scale of N, the running median routine should be applied with a width of $2N + 1$. Any deviant data from the running medians were then regarded as glitches. The scale of glitches was typically $N = 2$; a cosmic ray impact and its trailing remnant. A new glitch sometimes occurred

before the preceding glitch had faded out. To take account of such overlaps, the scale was set to $N = 3$. Thus, $2N + 1 = 7$ was set for the width of the running median. This cosmic ray masking routine was repeated until no data deviated from the threshold. Then, an additional masking was applied with a scale of $N = 11$, equivalent to the number of exposures at a raster point ($N_{\rm exp} = 12$).

This first masking step on the *dsub* data may mask bright objects. Thus, once the *sresp* data were derived without contamination from glitches, all the masks were canceled. New masks were then created from the *obj* data. To preserve object fluxes in this step, a median of all exposures at each raster point was calculated as a reference value for masking. For example, a median of the *i*th raster point was compared with all the data samples at this raster point. Any data samples which deviated from the threshold were masked out.

The reference values for the first and second masking steps were derived from two dozen samples at most. Many points of sky within our field were observed more than 1000 times. Thus, in the third masking step, the low noise *robj* data were utilized (Appendix A.3.2). All data in the *obj* data were compared with their respective *robj* data. Any data were masked if they deviated from the threshold.

Because we iterated the processing to refine object masks (Appendix A.3.3), the operation returned to the initial cosmic ray masking routine with the *dsub* data after the *robj* masking step. In the second iteration and later, only the scale $N = 2$, instead of 3 and 11, was used to deglitch the *dsub* data.

Different deglitching thresholds were set for cosmic ray impacts and their trailing remnants; typically 3 and 2.5 sigmas, respectively. These thresholds were adjusted to result in zero background in a map (Eq. (8)) and no loss in object fluxes. For discrimination of objects and cosmic rays, a standard deviation map and a median absolute deviation map (Eq. (A.2)) were compared. Objects appear in both maps while cosmic rays appear only in the standard deviation map. In the *robj* deglitching, an additional margin for the thresholds was set to go well with the median nature of the *robj* data (Fruchter & Hook 1998). At the final stage, cosmic ray masks occupy 23% of the data.

A.5. Sky brightness

The fiducial sky flux $I^0_{\rm sky}$ falling onto the fiducial pixels must be known to derive the object flux *obj* (Eq. (10)). The fiducial pixels are the central 12×12 detector pixels that have negligible effects from the optical distortion and the vignetting ($\alpha = 1$ in Eq. (9)). The sky flux was dominated by the zodiacal light and the zodiacal light depends on the solar aspect angle (Table 1). Thus, the sky flux must be measured for each revolution. The $I^0_{\rm sky}$ was determined in two steps: (1) a median value of each pixel in the *sresp* data was calculated to minimize the effect of the responsivity drifts, and then (2) these median values of the central 12×12 pixels were averaged. The fiducial sky flux for each revolution is given in Table 1, after the conversion to the sky brightness.

A.6. Map creation

There exists an offset between the image on the detector and the actual satellite pointing. This is due to jitter in the lens wheel repositioning in the camera. The offsets due to the jitter vary from revolution to revolution. To evaluate these offsets, a revolution map was first created from the *obj* data taken in each revolution. At first, we describe the creation of the revolution maps.

Information about the satellite position and the optical distortion at the ISOCAM detector were used to coadd the *obj* data. To take account of the rotation and the distortion of the 6 arcsec detector pixels on the sky, a map with 0.6 arcsec sub-pixels was created aligned with the J2000 system. The position and the orientation of the ISOCAM detector were obtained based on three angles defining the satellite status; RA, Dec, and Roll. Then, each detector pixel area on the sky map was defined with positions of the four corners of that pixel. The positions were derived with the optical distortion correction dependent on the lens position (Aussel 1998). Finally, the distortion corrected pixel was shrunk to its 85% (0.85^2 in area) and put into sub-pixels. This shrink operation recovers some information lost in the undersampling of the optical beam (Fruchter & Hook 1998).

The pointing stability within $T_{\rm int} = 20$ s was measured as 0.34 arcsec ($1\,\sigma$) on the average. Frames having displacements twice as large as this value were regarded as having been taken during slews of the satellite. Such frames were not used for the coaddition. The jitter of the lens wheel gave rise to a weakly illuminated area at some edges of the detector array. Pixels in such areas show 3 times larger noise in the error propagation calculations. They were masked out in the coaddition. The fraction of detector area affected by weak illumination depended on the lens position (Table 1); 3% of a detector frame for the *left* position and 1% for the *right*.

After the revolution maps were obtained, positions of bright sources identified in different revolutions were compared. Based on the relative offsets of 19 sources, offsets among revolutions were derived (Table 1). With the correction of these offsets to the RA and Dec angles of the satellite, the final map (Fig. 2) was calculated in the same way to obtain revolution maps. Here all the *obj* data in all the revolutions were used.

Note that the relative offsets of the 19 sources had a mean deviation of 0.13 pixel, 0.8 arcsec. If such uncertainty is acceptable, a priori jitter correction can be performed. Namely, the offset in the *M*-direction is 1 pixel for the *left* position and -1 pixel for the *right*. The offset in the raster *N*-direction is 0 (Table 1).

A.7. Unfolding noise contributions

The noise in the 7.2 arcsec beam was estimated to be typically 1.1 μJy/beam, with a use of a histogram for the correct absolute scaling of the noise. This noise includes detector, processing, and confusion noises. Here we tried to unfold these noise sources.

For estimating a confusion noise, we adopted an evolution model by Franceschini et al. (1997) because of the small

deviation of our counts from this model. For an extension toward fainter fluxes, we assumed a parameterized form for the Franceschini et al. model

$$N(>S) = \frac{2\,N_0}{\left(\frac{S}{S_0}\right)^{\alpha_1} + \left(\frac{S}{S_0}\right)^{\alpha_2}} \quad \text{(A.3)}$$

with a set of parameters $(\alpha_1, \alpha_2, S_0, N_0) = (0.70, 1.95, 20\,\mu\text{Jy}, 6.4 \times 10^3 \text{deg}^{-2})$. This formula represents the model quite well at fluxes less than 100 μJy. We generated test sources following this parameterized relation down to 0.05 μJy and distributed them randomly over the sky. The fluctuation in the 7.2 arcsec beam over this map was estimated with a histogram, giving 0.49 μJy/beam as a modal value.

Using this simulated data set, we created raw data and all the image processing was executed as in the processing simulations in Sect. 5.2. The resulting noise became 0.56 μJy/beam. The increase in noise should come from a contribution of the processing noise, because we have not used real ISOCAM data in this case. By subtracting the confusion noise above quadratically, the processing noise was estimated to be 0.28 μJy/beam.

As the total noise of the real ISOCAM data is 1.1 μJy/beam, the detector noise in the ISOCAM data should be 0.91 μJy/beam by a quadratical subtraction. It assures that our observations were dominated by the detector noise, i.e. readout and photon noises.

References

Altieri, B., Metcalfe, L., Kneib, J. P., et al. 1999, A&A, 343, L65

Aussel, H. 1998, ISOCAM LW Channel Field of View Distortion, HTTP/users/expl_lib/CAM/distortion.ps.gz

Aussel, H., Cesarsky, C. J., Elbaz, D., & Starck, J. L. 1999, A&A, 342, 313

Barger, A. J., Cowie, L. L., Sanders, D. B., et al. 1998, Nature, 394, 248

Barger, A. J., Cowie, L. L., & Sanders, D. B. 1999, ApJ, 518, L5

Bertin, E., & Arnouts, S. 1996, A&AS, 117, 393

Bertoldi, F., Carilli, C. L., Menten, K. M., et al. 2000, A&A, 360, 92

Biviano, A., Sauvage, M., Gallais, P., et al. 1998, The ISOCAM Dark Current Calibration Report, HTTP/users/expl_lib/CAM/darkdoc.ps.gz

Blommaert, J. 1998, ISOCAM Photometry Report, HTTP/users/expl_lib/CAM/photom_rep_fn.ps.gz

Cesarsky, C. J., Abergel, A., Agnese, P., et al. 1996, A&A, 315, L32

Condon, J. J. 1997, PASP, 109, 166

Coulais, A., & Abergel, A. 2000, A&AS, 141, 533

Cowie, L. L., Gardner, J. P., Hu, E. M., et al. 1994, ApJ, 434, 114

Cowie, L. L., Hu, E. M., & Songaila, A. 1995a, AJ, 110, 1576

Cowie, L. L., Hu, E. M., & Songaila, A. 1995b, Nature, 377, 603

Cowie, L. L., Songaila, A., Hu, E. M., & Cohen, J. G. 1996, AJ, 112, 839

Désert, F.-X., Puget, J.-L., Clements, D. L., et al. 1999, A&A, 342, 363

Driver, S. P., Fernandez-Soto, A., Couch, W. J., et al. 1998, ApJ, 496, L93

Flores, H., Hammer, F., Désert, F.-X., et al. 1999, A&A, 343, 389

Franceschini, A., Toffolatti, L., Mazzei, P., Danese, L., & de Zotti, G. 1991, A&AS, 89, 285

Franceschini, A., Aussel, H., Bressan, A., et al. 1997, The Far Infrared and Submillimetre Universe, ESA SP401, 159 [astro-ph/9707080]

Franceschini, A., Silva, L., Fasano, G., et al. 1998, ApJ, 506, 600

Fruchter, A. S., & Hook, R. N. 1998, A Method for the Linear Reconstruction of Undersampled Images [astro-ph/9808087]

Gehrels, N. 1986, ApJ, 303, 336

Goldschmidt, P., Oliver, S. J., Serjeant, S. B. G., et al. 1997, MNRAS, 289, 465

Hacking, P., & Houck, J. R. 1987, ApJS, 63, 311

Hogg, D. W. 2001, AJ, 121, 1207

Hughes, D. H., Serjeant, S., Dunlop, J., et al. 1998, Nature, 394, 241

Kessler, M. F., Steinz, J. A., Anderegg, M. E., et al. 1996, A&A, 315, L27

Monet, D., Bird, A., Canzian, B., et al. 1998, USNO-A V2.0, A Catalog of Astrometric Standards, U.S. Naval Observatory Flagstaff Station (USNOFS) and Universities Space Research Association (USRA) stationed at USNOFS

Moneti, A., Metcalfe, L., & Schulz, B. 1997, Reference Wavelengths for ISO: CAM and PHOT Filters, HTTP/users/expl_lib/ISO/docs/ref_lam/

Mushotzky, R. F., Cowie, L. L., Barger, A. J., & Arnaud, K. A. 2000, Nature, 404, 459

Ochsenbein, F. 1997, Baltic Astron., 6, 221

Okumura, K. 1998, ISOCAM PSF REPORT, HTTP/users/expl_lib/CAM/psf_rep.ps.gz

Oliver, S. J., Goldschmidt, P., Franceschini, A., et al. 1997, MNRAS, 289, 471

Oliver, S., Mann, R. G., Carballo, R., et al. 2002, MNRAS, 332, 536

Pearson, C. 2001, MNRAS, 325, 1511

Primack, J. R., Bullock, J. S., Somerville, R. S., et al. 1999, Astroparticle Physics, 11, 93

Renault, C., Barrau, A., Lagache, G., et al. 2001, A&A, 371, 771

Roman, P., & Ott, S. 1999, Report on the behaviour of ISOCAM LW Darks, HTTP/users/expl_lib/CAM/dark_report.ps.gz

Rowan-Robinson, M. 2001, ApJ, 549, 745

Sato, Y., Cowie, L. L., Kawara, K., et al. 2002, ApJ, 578, L23

Sato, Y., Cowie, L. L., Kawara, K., et al. 2003, AJ, submitted

Serjeant, S. B. G., Eaton, N., Oliver, S. J., et al. 1997, MNRAS, 289, 457

Siebenmorgen, R., Sauvage, M., & Levine, D. 1996, Addendum to ISOCAM Observer's Manual, HTTP/manuals/CAM_add/doc.html

Silva, L., Granato, G. L., Bressan, A., & Danese, L. 1998, ApJ, 509, 103, http://grana.pd.astro.it/grasil/grasil.html

Smail, I., Ivison, R. J., & Blain, A. W. 1997, ApJ, 490, L5

Steidel, C. C., Giavalisco, M., Pettini, M., Dickinson, M., & Adelberger, K. L. 1996, ApJ, 462, L17

Taniguchi, Y., Cowie, L. L., Sato, Y., et al. 1997, A&A, 328, L9

Xu, C. K., Lonsdale, C. J., Shupe, D. L., et al. 2003, ApJ, 587, 90

Note: HTTP = http://www.iso.vilspa.esa.es